Shang *et al. Biochar* (2026) 8:92
https://doi.org/10.1007/s42773-026-00597-w

Biochar

ORIGINAL RESEARCH Open Access

Geoconductor function of graphitized biochar redirects microbial Fe(III) reduction and stimulates hydroxyl radical production in paddy soil

Hua Shang[1,2], Chao Jia[2], Song Wu[2], Ning Chen[2], Yujun Wang[2] and Xiangdong Zhu[2*]

Abstract

Integrating biochar into paddy soil as a hybrid geobattery–geoconductor material offers a transformative approach for sustainable soil decontamination. However, biochar often has an undeveloped graphitized structure and poor geoconductor function, restricting the electron transfer capacity for microbial Fe(III) reduction and subsequent •OH generation. In this study, the flash Joule heating method was used to enhance the graphitized structure of biochar to redirect microbial Fe(III) reduction via a geoconductor function-induced electron self-adaptation pathway. Specifically, a highly conductive framework of graphitized biochar (G-biochar) with a 2.64-fold enhancement in electrical conductivity unchoked the electron transfer obstacle between Fe(III)-reducing bacteria (*Bacillus*, *Anaeromyxobacter*, *Citrifermentans*, and *Flavisolibacter*) and Fe(III), This mechanistic improvement resulted in 18.9% increase in active Fe(II) generation. Accordingly, 54.9% increase in •OH production and 57.2% increase in the sulfamethoxazole degradation rate were evidenced. Finally, G-biochar differentially promoted microbial Fe(III) reduction in various paddy soils, which mainly depended on the activity of the reducing microbial community. These findings redefine the biochar trade-off effect on soil microbial–geochemical processes via the geoconductor function rather than the previously acknowledged geobattery electron reservoir mixing strategy.

Highlights

- Graphitized biochar redirects direct electron transfer from bacteria to Fe(III).
- Graphitized biochar increased Fe(II) production by 18.9% via geoconductor function.
- Graphitized biochar boosted •OH production and SMX degradation by 54.9% and 57.2%, respectively.
- Graphitized biochar functions as a geoconductor, redefining its role beyond geobattery.

Keywords Biochar, Electron transfer, Geoconductor, Soil microbial Fe(III) reduction, Hydroxyl radicals

*Correspondence:
Xiangdong Zhu
xdzhu@issas.ac.cn
Full list of author information is available at the end of the article

Springer

Graphical Abstract

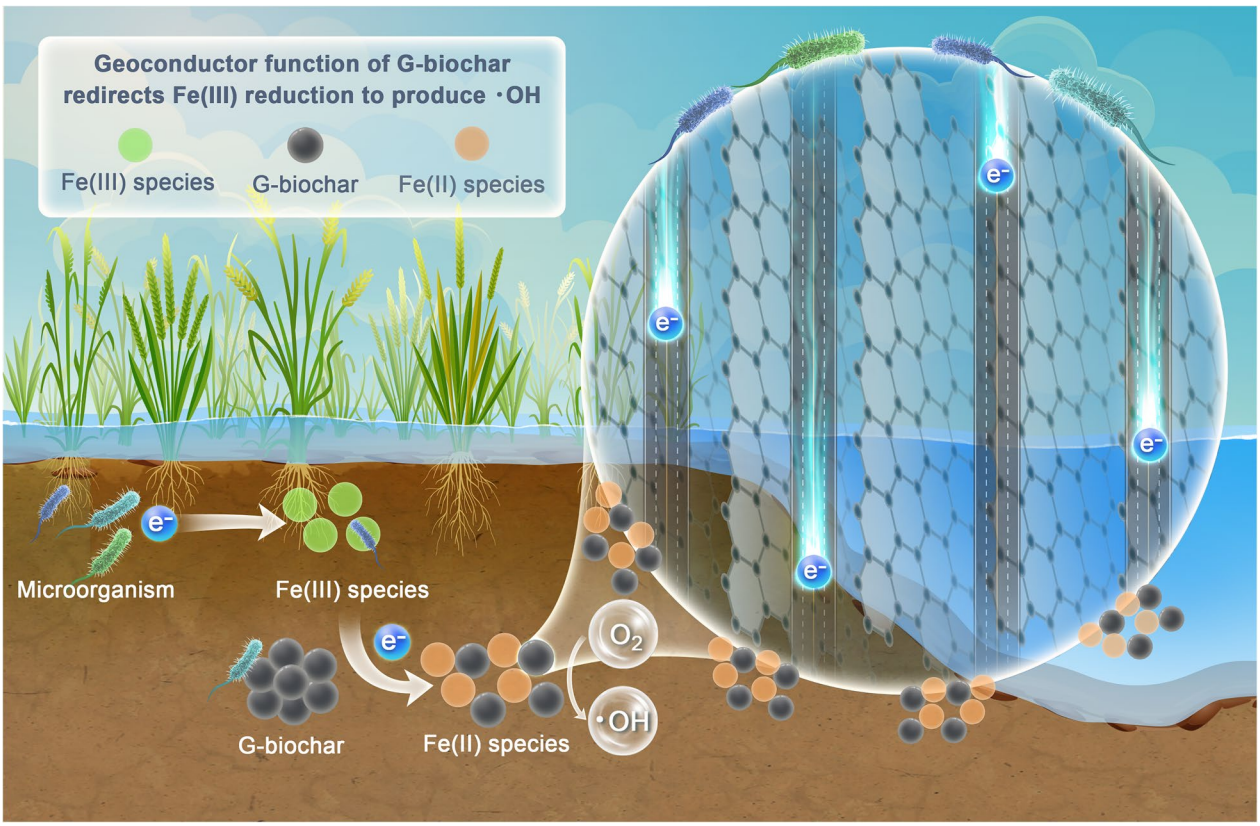

1 Introduction

Paddy soils continuously receive input of livestock manure and slightly polluted irrigation water; thus, organic pollutants, such as antibiotics, are frequently detected at high concentrations of 0.1–3.5 mg kg^{-1} (Wei et al. 2021; Wu et al. 2024a). These concentrations significantly exceed the critical threshold of natural attenuation capacity (Chen et al. 2024b). Therefore, accelerating free radical activation (such as •OH) to drive redox reactions and degrade organic pollutants in paddy soils during redox fluctuations has become a pivotal strategy for addressing agro-environmental pollution (Huang et al. 2023; Yuan et al. 2018; Zeng et al. 2020; Zhang et al. 2016). •OH generation is strongly affected by active Fe(II) species, which mainly originate from microbial Fe(III) reduction (Page et al. 2013, 2012; Tong et al. 2016). Although continuous Fe(II) generation is inevitably influenced by complex environmental factors (Chen et al. 2024a; Ginn et al. 2017), it is primarily constrained by microbe-mediated electron transfer pathway and reduction activities (Gligorovski et al. 2015; Pan and Chu 2016).

Biochar has recently emerged as a hybrid geoconductor–geobattery material in paddy soil systems that strengthens •OH formation by mediating electron transfer between Fe minerals and soil microbes (Sun et al. 2017). Biochar with graphitized structures functions as a geoconductor due to its excellent electrical conductivity, which facilitates long-range electron transport between spatially separated redox zones—akin to a "microbial nanowire" at the macroscale (Wu et al. 2021). The geobattery function of biochar stems from the quinone/phenolic group (C=O/ C–OH) that acts as an electron reservoir, enabling the storage and regulation of electron release with charging and discharging cycles for microbial Fe(III) reduction (Xu et al. 2025; Yu et al. 2022). Currently, the trade-off effect of biochar on soil microbial geochemical processes is realized primarily through the oxygen-containing functional groups that exert the geobattery function (Lee et al. 2023; Sun et al. 2018).

It is well known that graphitized structures are foundational to effective electron transfer (Sun et al. 2018; Yang et al. 2024). Notably, the oxygen-containing functional groups and graphitized structures represent two contradictory aspects of electron transfer in biochar. Although the oxygen-containing functional groups can store electrons, they disrupt the conjugated electron system and block electron transfer (Strauss et al. 2018). In contrast, the graphitization structure facilitates electron tunneling interactions between clusters in the graphite region (sp^2 carbon) (Qiu et al. 2023). Consequently, although the oxygen-containing functional groups enable the storage and release of electrons through charging–discharging cycles, the electron transfer remains fundamentally dependent on the graphitization structures (Zhu et al. 2025).

To overcome the obstacle to electron transfer associated with the oxygen-containing functional groups, emerging strategies have focused on reconstructing the biochar graphitization structure through flash Joule heating (FJH) (Barbhuiya et al. 2021; Luong et al. 2020). FJH transformation can establish an electronic highway and unchoke the electron transfer obstacle between reducing bacteria and Fe(III). In this study, we synthesized graphitized biochar (G-biochar) using the FJH method to improve the graphitized structure and, ultimately, its geoconductor function. The geoconductor function-induced electron self-adaptation pathway should improve electron transfer and microbial Fe(III) reduction, ultimately enhancing •OH generation. Finally, we investigated the applicability of G-biochar for enhancing •OH generation in various paddy soils.

2 Materials and methods

2.1 Chemicals and paddy soils

Sources of chemicals are included in Text S1. Soil samples (0–20 cm topsoil) were randomly collected for each plot using a diameter auger with litter, herbs, and rocks removed. The black soil samples were collected from paddy sites of Changchun in Jilin province, China. The cinnamon soil samples were collected at Xianning in Hubei province, China. The red soil samples were gathered at Shangrao in Jiangxi province, China. More physicochemical properties of paddy soils are listed in Table S1. To maintain the physicochemical properties and microbial community composition, the paddy soil samples were air-dried in the dark for preservation. Air-dried soil was sieved through a 2 mm sieve to further remove plant residues. Then, the paddy soils were incubated under anoxic conditions to reconstitute their microbial activity for 14 days.

Moreover, to confirm the role of paddy soil microorganisms in paddy soil Fe(III) reduction, soil samples were sterilized by the γ-ray sterilization method. Soil samples were sterilized for 40 h at a rate of 50 krad h^{-1} for a total γ-ray dosage of 20 kGy. In addition, sulfamethoxazole (SMX), as a common antibiotic that contaminates agricultural soils, was chosen as a model pollutant for further investigation.

2.2 Preparation of biochar and graphitized biochar

Biomass bamboo was employed for biochar and G-biochar production. Briefly, the biomass bamboo was crushed into powder (80 mesh) and carbonized into biochar at 700 °C pyrolysis temperature with a 60-min hold time. Then, the FJH method was employed to upgrade the biochar to G-biochar (Teng et al. 2023; Yu et al. 2023a). The G-biochar obtained from the biochar was upgraded by FJH treatment using a self-made system (Fig. S1). The details of FJH method to prepare G-biochar are described in Text S2. It should be emphasized that the flash Joule heating (FJH) process leverages the Joule heating effect of electric current to instantaneously generate ultra-high temperature, thereby achieving rapid carbonization of materials (Fig. S2).

2.3 Characterizations of biochar and graphitized biochar

In Raman spectra, three distinctive Lorentz peaks were fitted at D (~1350 cm^{-1}), G (~1580 cm^{-1}), and 2D (~2700 cm^{-1}) bands using Lab-Spec6.4 software. X-ray photoelectron spectroscopy (XPS) was performed on biochar and G-biochar using Thermo ESCALAB 250 XI with Al Kα X-ray radiation (400 μm spot size). Survey scans were acquired with a pass energy of 50 eV and a step size of 0.05 eV. The binding energies of high resolutions spectra were calibrated using the C 1 s peak at 284.8 eV. The flake thickness of biochar and G-biochar was determined using an atomic force microscope (AFM, Asylum Research MFP-3D, USA).

2.4 Electrochemical analysis of biochar and graphitized biochar

Cyclic coltammetry (CV) CV spectra were conducted in three-electrode electrochemical cells using a CHI660A electrochemical workstation (CH Instruments, USA). A glassy carbon electrode (Φ = 3 mm), a platinum wire, and a saturated Ag/AgCl served as the working, counter, and reference electrodes, respectively. During the electrochemical tests, the electrolyte (0.1 M phosphate and 0.1 M KCl, pH 7.0) was saturated with N_2 to eliminate O_2 and its interference. The details of the CV spectra characterization of biochar samples are described in Text S3.

Mediated electrochemical analysis The electron donating capacity (EDC) and electron accepting capacity (EAC) of biochar and G-biochar were characterized by mediated electrochemical oxidation (MEO) and

reduction (MER), respectively, using chronoamperometric experiments. The working electrode was poised at + 0.41 V and −0.69 V, and 2,2′-azino-bis(3-ethylbenzothiazoline-6-sulfonic acid) diammonium salt (ABTS) and zwitterionic viologen 4,4′-bipyridinium-1,1′-bis(2-ethylsulfonate) (ZiV) served as the electron transfer mediators during the EDC and EAC measurements, respectively. All these solutions were purged with N_2 to eliminate dissolved oxygen. In the chronoamperometric experiments, when the working electrode was held at a potential in 30 mL of electrolyte with stirring, a background current response which became steady was noticed. After constant background currents were rebalanced, 100 μL of samples were injected into the working electrode. The number of electrons transferred to postreaction samples was quantified by integration of reductive and oxidative current responses in MER and MEO.

Electrical conductivity analysis Electrical conductivity (EC) of biochar and G-biochar was measured using a powder resistivity testing instrument (FM100GH, Honghu Testing Instrument Co. Ltd., Xi'an, China). The resistivity (ρ) was recorded at 10 MPa, and the reciprocal of the resistivity is EC (σ) (i.e., $\sigma = 1/\rho$) (Yang et al. 2024; Yu et al. 2022). For galvanostatic charge and discharge experiments, the galvanostatic charge was set at 0.0001 A and cycled six times.

2.5 Redox alternating cycles with biochar and graphitized biochar

After incubation, wet soils were weighed into 100 mL serum bottles based on their moisture, to achieve a system consisting of 10 g of soil (dry weight) and 50 mL of deoxygenated deionized water (99.9% N_2, 1 h) containing SMX with desired concentration.

For the anoxic period, after incubation, the bottle was purged with N_2 for 30 min to simulate anoxic condition. The bottle was sealed and then shaken in the dark for 12 h. Afterward, for the oxic period, the bottle was purged with air for 30 min to simulate oxic condition and start the oxic period, during which the bottle was open to air to ensure sufficient O_2 for 12 h. Similarly, after the reaction, the headspace was purged with N_2 for 30 min to simulate anoxic condition. In total, these anoxic–oxic alternating systems were performed over five cycles, the first (0–24 h), the second (24–48 h), the third (48–72 h), the fourth cycle (72–96 h), and the fifth cycle (96–120 h) (Zhang et al. 2024). During the reaction process, 0.5 mL of the solution was sampled at regular intervals, and 2 mL of methanol was added to terminate the reaction and extract SMX. The extracted slurries were separated and filtrated by 0.22 μm membrane filter. The recovery rates of SMX from paddy soil ranged from 93.2 to 97.5%.

2.6 •OH production capacity of paddy soils

To determine the •OH concentration, separate experiments were conducted with sodium benzoic acid (BA) instead of SMX since BA reacts with •OH to generate *p*-hydroxybenzoic acid (*p*-HBA) during oxygenation. The concentration of *p*-HBA was quantified by high-performance liquid chromatograph (HPLC). Further, the concentration of $O_2^{\bullet-}$ was quantified with the yellow nitroblue tetrazolium (NBT) method due to its sensitivity to $O_2^{\bullet-}$. Briefly, NBT was reduced to blue formazan by $O_2^{\bullet-}$ due to the stronger reduction potential of $O_2^{\bullet-}$ than NBT (−0.33 vs −0.05 V). Theoretically, 1 mol of NBT could react with 4 mol of $O_2^{\bullet-}$. The concentration of the generated $O_2^{\bullet-}$ in the suspension was measured by recording the residual concentration of NBT at 259 nm by a UV–vis spectrophotometer. Besides, to determine the contribution of •OH and $O_2^{\bullet-}$ to SMX degradation, quenching experiments were carried out by adding catalase (CAT) and superoxide dismutase (SOD), respectively.

2.7 Fe(II) species identification during paddy soils microbial Fe(III) reduction

Sequential extraction was applied to analyze Fe(II) species in soil (Huang et al. 2023). The soil samples were sequentially extracted using 1 M $CaCl_2$, 0.5 M HCl, 5 M HCl, and 1.3 M HF to obtain (i) exchangeable Fe, (ii) surface-bound or complexed Fe and Fe in low-crystalline minerals (e.g., siderite and green rust-like phase), (iii) highly crystalline Fe-bearing minerals (e.g.,hematite), and (iv) Fe in silicates and clays, respectively (Chen et al. 2021). These were defined as ion exchangeable, surface-bound, mineral structural, and phyllosilicate Fe, respectively. Concentration of Fe(II) was measured at 510 nm using a modified phenanthroline method on a UV–vis spectrometer (MAPADA UV2550), with the detection limit of 5 μM.

2.8 Microorganism community analysis of paddy soils

To investigate the effect of biochar samples on microbial Fe(III) reduction in paddy soil, bacterial communities were characterized based on amplicon sequencing analysis. Triplicates were performed for each treatment. Details of DNA extraction, 16S rRNA gene sequencing, and soil bacterial community characterization are provided in the Supporting Information section of this paper (Text S4).

3 Results and discussion

3.1 Structural properties of graphitized biochar for geoconductor function verification

The biochar and G-biochar structures were analyzed to verify the changes in the electronic properties. The

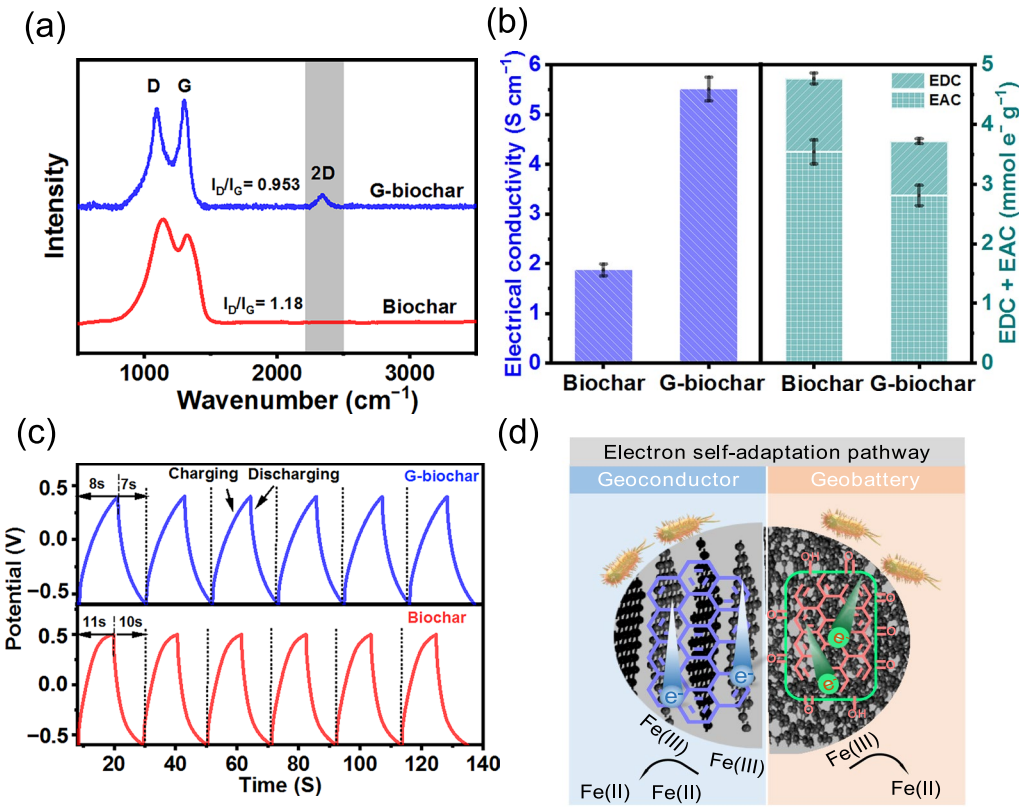

Fig. 1 The structure and electrochemical analyses of biochar and graphitized biochar (G-biochar). **a** Raman spectrum of biochar and G-biochar. **b** Electrical conductivity, electron-donating capacity (EDC), and electron-accepting capacity (EAC) of biochar and G-biochar. **c** Galvanostatic charge and discharge curves of biochar and G-biochar. **d** The mechanism diagram of electron transfer of biochar and G-biochar

intensity ratio of the D-to-G peaks (I_D/I_G) decreased between biochar and G-biochar (Fig. 1a), indicating a more graphitized structure in G-biochar. The AFM analysis suggested that the FJH reaction reformed the amorphous carbon framework of the biochar into one with fewer carbon layers of G-biochar (Fig. S3). The formation of the graphitization structure in G-biochar was primarily attributed to the Joule heating-induced graphitization and simultaneous exfoliation of the graphite through current-induced stress (Teng et al. 2023; Wang et al. 2017). Moreover, the G-biochar showed decreased reduction and oxidation peaks in the CV curves, indicating a weak electron storage (geobattery) capacity (Fig. S4). This result suggested that there were few functional groups in the G-biochar, as confirmed by the XPS spectra (Fig. S5). After the FJH reaction, the oxygen-containing functional groups on the surface of the G-biochar decreased (Fig. S5). Notably, the C=O ratio remained stable, whereas that of C–O decreased slightly from 18.7% to 7.92%. Overall, it can be inferred that the G-biochar with the graphitized structure featured an inferior electron storage (geobattery) function compared to biochar due to fewer oxygen-containing functional groups.

The alterations in the graphitized structure and surface functionality exert diverse impacts on the electrochemical properties of biochar and G-biochar (Xu et al. 2025). The electrical conductivity of G-biochar (5.51 ± 0.24 S cm^{-1}) was much higher than that of biochar (1.87 ± 0.12 S cm^{-1}) (Fig. 1b). The increased electrical conductivity implied superior direct electron transfer (geoconductor) capacity compared to biochar (Li et al. 2024). Further, the EAC values in the MER system were 3.54 ± 0.2 and 2.81 ± 0.17 mmol e^- g^{-1}, while the corresponding EDC values in the MEO system were 1.23 ± 0.09 and 0.91 ± 0.04 mmol e^- g^{-1} for biochar and G-biochar, respectively (Fig. 1b and S6). Therefore, the EEC values of biochar and G-biochar were 4.77 ± 0.29 and 3.72 ± 0.21 mmol e^- g^{-1}, respectively. Notably, the biochar exhibited a higher EEC than G-biochar, which could be attributed to its intensive surface functionality. This result further suggests that G-biochar has an inferior electron storage (geobattery) capability compared to biochar. We evaluated the stability of the capacitance between the galvanostatic charge and discharge (GCD) rates of the biochar and G-biochar (Fig. 1c). Both biochar and G-biochar presented a stable symmetric

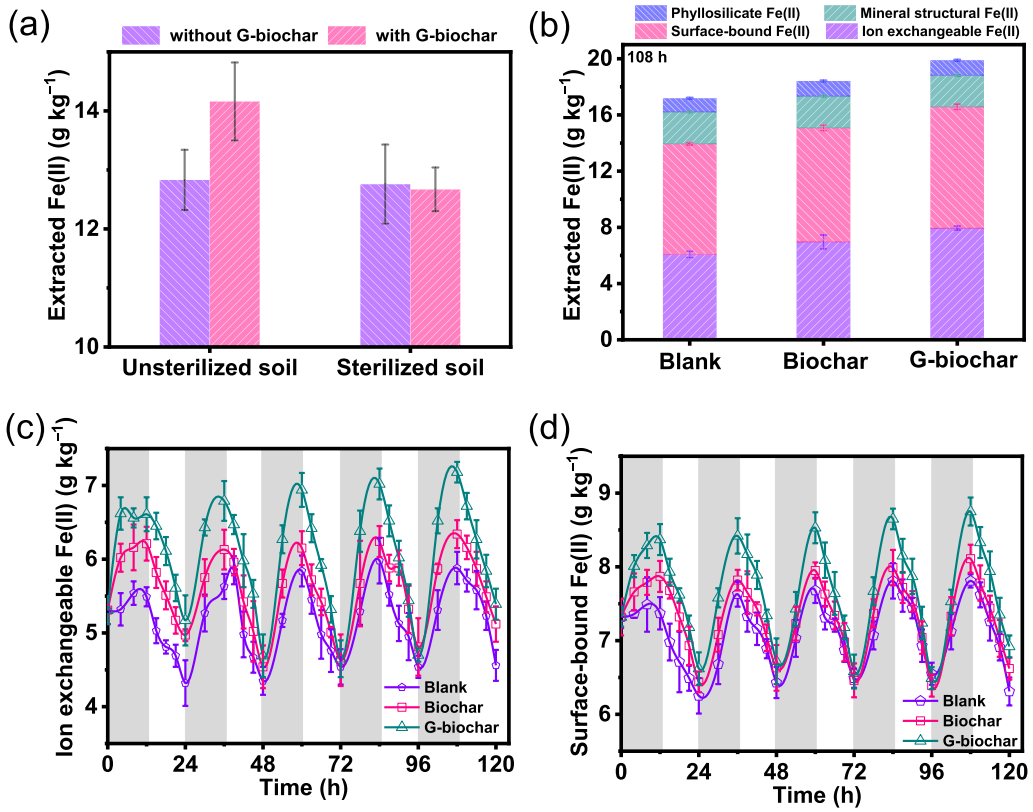

Fig. 2 Fe(II) species transformation during, reaction in paddy soils (black soil) during redox fluctuation. **a** Contents of Fe(II) species in unsterilized and sterilized paddy soils with and without G-biochar. **b** Contents of Fe(II) species in paddy soils amended with biochar and G-biochar after 120 h of reaction. **c** Variation of ion exchangeable Fe(II) species in soils amended with biochar and G-biochar during the reaction under redox fluctuation. **d** Variation of surface-bound Fe(II) species within biochar and G-biochar during the reaction under redox fluctuation

isosceles-like GCD curve. However, the charge and discharge times of G-biochar (8 and 7 s) were shorter than those of biochar (11 and 10 s). These results suggest that the geobattery function is dominant in biochar, whereas the geoconductor function predominates in G-biochar. Therefore, G-biochar can facilitate soil microbial geochemical processes via a geoconductor function-based mixing strategy (Fig. 1d).

3.2 Geoconductor function of graphitized biochar redirects microbial Fe(III) reducing

To confirm the role of soil microorganisms in paddy soil Fe(III) reduction, soil samples were sterilized through γ-ray sterilization. G-biochar facilitated Fe(II) formation in unsterilized paddy soils but not in sterilized soils (Fig. 2a), demonstrating that the graphitized biochar structure affected the soil microbial Fe(III) reduction process. Hence, we examined Fe(II) formation during microbial Fe(III) reduction in paddy soils to verify the role of G-biochar as a geoconductor. G-biochar enhanced active Fe(II) formation with 18.9% increase in paddy soils after 108 h of reaction compared with the blank treatments (Fig. 2b and S7), suggesting that G-biochar promoted microbial Fe(III) reduction. The graphitization structure greatly affected the concentrations of active surface-bound and ion-exchangeable Fe(II) species (Fig. S8). Specifically, the surface-bound and ion-exchangeable Fe(II) contents at 108 h increased from 8.01 g kg^{-1} and 6.34 g kg^{-1} in biochar to 8.63 g kg^{-1} and 7.18 g kg^{-1} in G-biochar, respectively (Fig. 2c, d). This is primarily because the geoconductor function of the G-biochar provides superior electron transfer capability compared to biochar. These results indicate that G-biochar primarily facilitates electron transfer via its geoconductor function, thereby diverting microbial Fe(III) reduction and increasing active Fe(II) species generation (Shen et al. 2025).

To explore the effects of G-biochar on paddy soil microbial communities, high-throughput sequencing of soil samples was performed after the reaction (Chen et al. 2024a). As shown in Fig. 3a, G-biochar increased the alpha diversity relative to the blank and biochar treatments. The principal coordinate analysis of the weighted UniFrac distances showed that the bacterial communities were separated between treatments (Fig. 3b). These

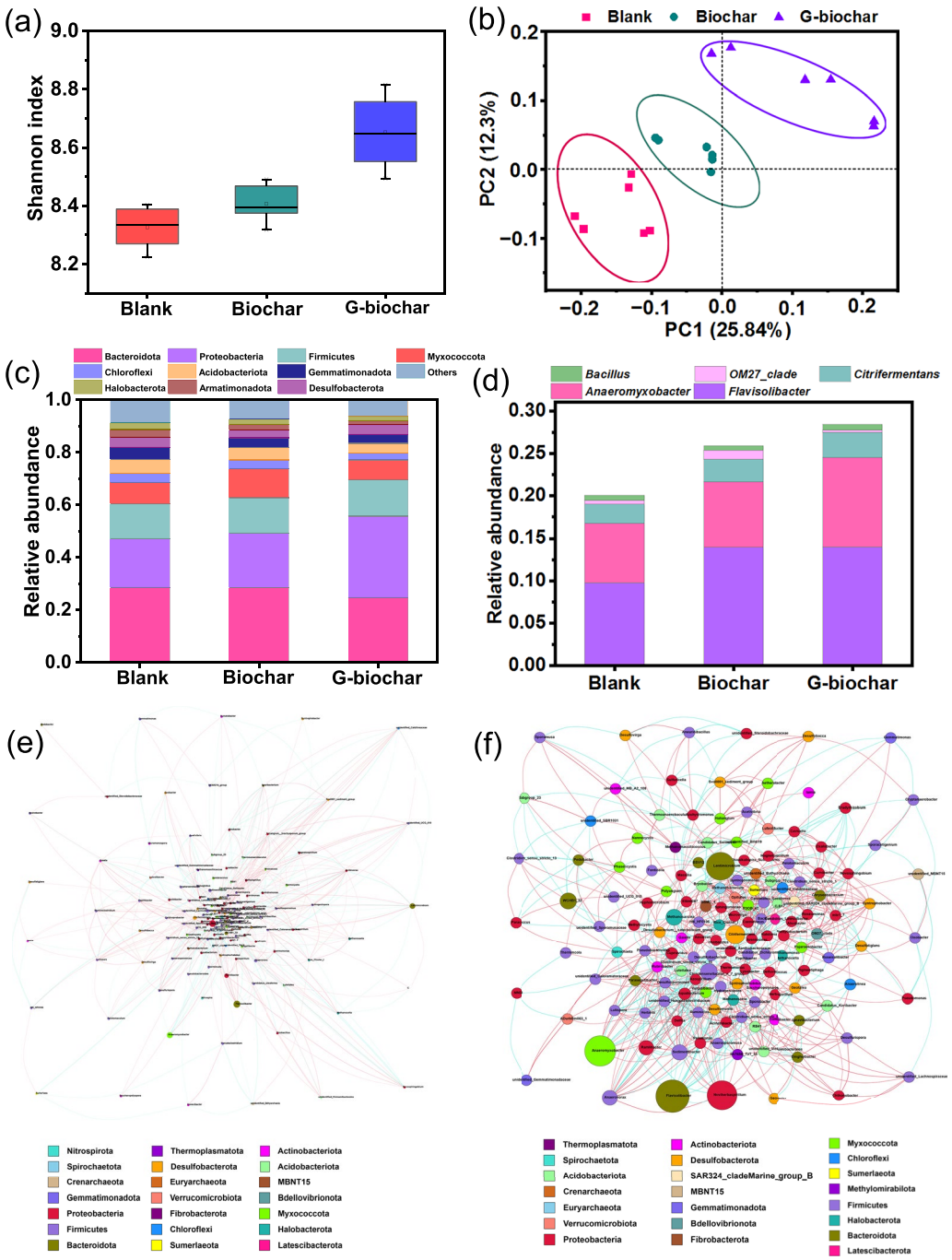

Fig. 3 Microbial responses of bacteria in paddy soils (black soil) within biochar and G-biochar at the phyla and genus level. **a** Alpha diversity index (Shannon index) of the bacterial community. **b** Principal Co-ordinates Analysis (PCoA) of the bacterial community. **c** Relative abundance of total bacterial communities at the phylum level in paddy soils amended with biochar and G-biochar. **d** Relative abundance of identified Fe(III)-reducing bacteria at genus level in paddy soils amended with biochar and G-biochar. Co-occurrence networks of bacterial communities in paddy soils (black soil) amended with **e** biochar and **f** G-biochar. A connection stands for a significant ($p < 0.05$) correlation between two nodes. Different nodes represent various genera. The size of each node is proportional to the connection numbers (i.e., degree), and the thickness of each connection (i.e., edge) is proportional to Pearson correlation coefficients. The red edge indicates positive interaction, while the green edge means negative interaction

results imply that G-biochar promotes the diversity of soil microbial communities (Chen et al. 2024a; Zhou et al. 2023). To better understand the microbial communities changes induced by biochar and G-biochar, we calculated the relative abundance of the 10 dominant phyla relative to the blank treatment (Fig. 3c). The microbial phyla mainly included Bacteroidota (22.4–30.6%), Proteobacteria (14.4–23.0%), and Firmicutes (9.3–10.7%). G-biochar was associated with a higher relative abundance of Proteobacteria (18.6% to 31.1%) and Firmicutes (12.8–13.9%) but lower abundance of Bacteroidota (28.6–24.7%), and Myxococcota (8.17–7.39%) (Fig. 3c). Among the most abundant genera, *Bacillus*, *Anaeromyxobacter, OM27*_clade, and *Flavisolibacter* were the main Fe(III)-reducing bacteria (Fig. 3d and S9). G-biochar increased the relative abundance of Fe(III)-reducing bacteria, indicating that it recruits the dominant conducive strains (Zhou et al. 2019). G-biochar's conductivity makes this electron flow so rapid that it relieves metabolic bottlenecks for both organisms (Wu et al. 2024b): *Anaeromyxobacter* gains a superior respiratory pathway, while *Bacillus* benefits from the constant demand for its fermentation products. In short, G-biochar selects for and enriches this specific consortium by wiring their metabolisms together into a highly efficient circuit for energy production.

Further, in the redox fluctuation system, G-biochar decreased the Eh value, consistent with the rapid increase in Fe(III)-reducing bacterial abundance (Fig. S10). This demonstrated that G-biochar could accelerate microbial Fe(III) reduction via increasing the abundance of Fe(III)-reducing bacteria. In addition, G-biochar increased the positive portions of the linear relationship based on the microbial network analysis (Fig. 3e, f). These findings suggest that soil enrichment with the geoconductor-dominant G-biochar can enrich reducing microbe abundance and thereby drive microbial Fe(III) reduction.

Although biochar can store electrons from soil microorganisms via its geobattery function, it cannot transfer electrons to the acceptor Fe(III) via the geoconductor function (Yu et al. 2023b). In addition, the geobattery function associated with redox-active functional groups is sensitive to pH and dissolved organic matter in complex soil systems, whereas the geoconductor function provides a more stable and persistent electron transfer pathway (Shen et al. 2025). Interestingly, the G-biochar with dominant geoconductor function greatly promoted microbial Fe(III) reduction. Therefore, transferring electrons through the geoconductor function rather than the geobattery function is an important pathway for facilitating microbial Fe(III) reduction. This demonstrates the electronic adaptive pathway in which electrons select the most favorable transfer path based on the soil environment during microbial Fe(III) reduction. On the other hand, G-biochar promotes the relative abundance of Fe(III)-reducing bacteria, suggesting that more electron donors existed in this process. Hence, the geoconductor-dominant G-biochar recruited Fe(III)-reducing microorganisms, creating a self-reinforcing cycle by which these enriched microbes reciprocally enhance electron supply. Overall, G-biochar can facilitate microbial Fe(III) reduction via its geoconductor function and the enrichment of reducing microbe abundance.

3.3 Geoconductor function of graphitized biochar enhances •OH formation

The G-biochar exhibited improved •OH production by 54.9% (1.34 μM g^{-1} soil), while biochar showed a slight increase of 17.1% (1.01 μM g^{-1} soil; Fig. 4a). These results suggest that G-biochar enhances •OH formation to a greater extent than biochar (Wu et al. 2017). The correlation analysis showed that the oxidized Fe(II) content was positively correlated with increased •OH accumulation in bulk soils for all reaction cycles (Fig. 4b). This indicates that G-biochar accelerates •OH formation via promoting microbial Fe(III) reduction. Figu. S11 shows a decrease in •OH accumulation in sterilized soil with G-biochar, suggesting that G-biochar only has an impact on microbial Fe(III) reduction and does not affect Fe(II)-induced oxygen activation. Based on the above results, it can be concluded that G-biochar accelerates Fe(II) generation via its superior geoconductor function, finally promoting subsequent •OH formation (Yang et al. 2021).

To confirm the •OH generation pathway, quenching experiments were performed using CAT and SOD as efficient scavengers of $O_2^{\bullet-}$ and H_2O_2, respectively (Fig. 4c). The almost equal inhibition of •OH formation by CAT and SOD indicated that $O_2^{\bullet-}$ and H_2O_2 were the intermediate products of •OH (Liu et al. 2024). To verify the concentration of $O_2^{\bullet-}$, chemical-probing experiments were performed using NBT as a probe for $O_2^{\bullet-}$ (Fig. S12). The $O_2^{\bullet-}$ concentration increased with reaction time, consistent with the formation of •OH. This suggests that $O_2^{\bullet-}$ and H_2O_2 are the intermediate products of •OH formation in G-biochar (Huang et al. 2023).

After 120 h of reaction, the degradation rate of SMX during redox fluctuation was 100.0% with G-biochar, 79.8% with biochar, and 46.3% with the blank treatment (Fig. 4d). This implies that G-biochar facilitates electron transfer via its superior geoconductor function (Yang et al. 2021), leading to increased •OH formation and SMX degradation. The effects of the initial SMX concentration, G-biochar dose, and pH on SMX degradation

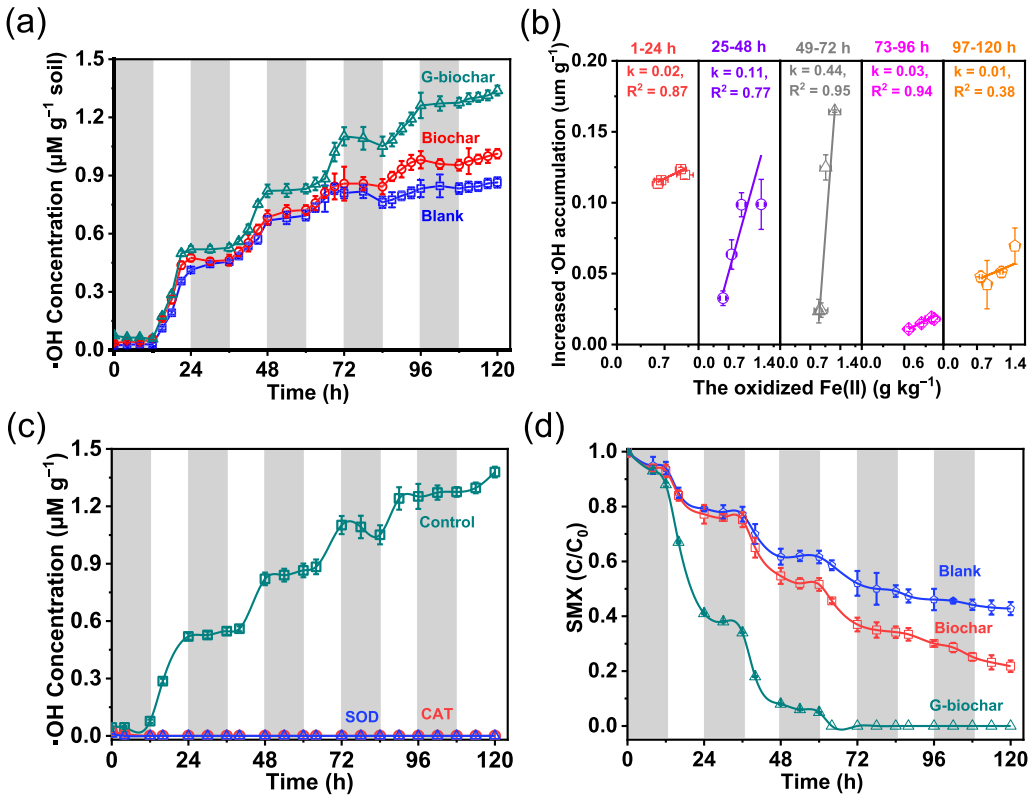

Fig. 4 ·OH formation and sulfamethoxazole (SMX) degradation in paddy soils (black soil). **a** Comparison of ·OH accumulation in paddy soils amended with biochar and G-biochar during redox fluctuation. **b** Correlation analysis between the contents of oxidized Fe(II) and increased ·OH accumulation in paddy soils amended with G-biochar during redox fluctuation ($p < 0.05$). **c** Quantification of ·OH with catalase (CAT) and superoxide dismutase (SOD). **d** Comparison of sulfamethoxazole (SMX) degradation during redox fluctuation. [dose of G-biochar sample = 10 g kg^{-1}, SMX concentration = 5 mg L^{-1}, pH = 5.0, soil to water ratio: 1/5 (w/w)]

were further investigated. Increasing the initial SMX concentration from 1 to 50 mg L^{-1} significantly decreased the SMX degradation efficiency from 100.0% to 78.4% (Fig. S13). The addition of G-biochar from 1 to 100 g kg^{-1} dramatically enhanced the SMX degradation efficiency from 77.6% to 100.0%. Furthermore, a decrease in pH (to acidic levels) also contributed to SMX degradation.

3.4 Application of graphitized biochar on various paddy soils

G-biochar enhanced ·OH production in all paddy soils (Fig. 5a), specifically increases of 14.5% (0.22 μM g^{-1} soil) in red soil, 21.4% (0.45 μM g^{-1} soil) in cinnamon soil, and 57.1% (1.33 μM g^{-1} soil) in black soil were observed. This indicated that G-biochar can accelerate ·OH formation differently in various paddy soils. Similar increases were observed in the content of active Fe(II) (surface-bound and ion-exchangeable) species (Fig. 5b). The concentrations of active Fe(II) species varied greatly in all paddy soils during the reaction (Fig. S14). Specifically, surface-bound Fe(II) content at 120 h increased from 4.75 g kg^{-1} in red soil to 6.71 g kg^{-1} in black soil, and ion exchangeable Fe(II) content at 120 h increased from 3.16 g kg^{-1} in red soil to 4.76 g kg^{-1} in black soil (Fig. S14). These results imply that the changes in Fe(III) reduction induced by G-biochar are related to soil properties (such as soil microbes) (Shen et al. 2025).

The bacterial communities of all paddy soils were investigated to explain the differences in microbial Fe(III) reduction and subsequent ·OH production associated with G-biochar. Black soil showed the largest alpha diversity relative to red and cinnamon soil (Fig. S15). The principal co-ordinates analysis showed that the bacterial communities differed between treatments (Fig. S16). These results imply that the different paddy soils have clearly different microbial communities. The bacterial communities mainly comprised Actinobacteriota (15.6–22.0%), Chloroflexi (15.6–17.3%), and Proteobacteria (14.4–23.0%) at the phylum level (Fig. 5c). Furthermore, the relative abundances of Firmicutes and Desulfobacterota increased from red to black soil, while that of Acidobacteriota and Planctomycetota decreased (Fig. 5c). At the genus level, the relative abundance of

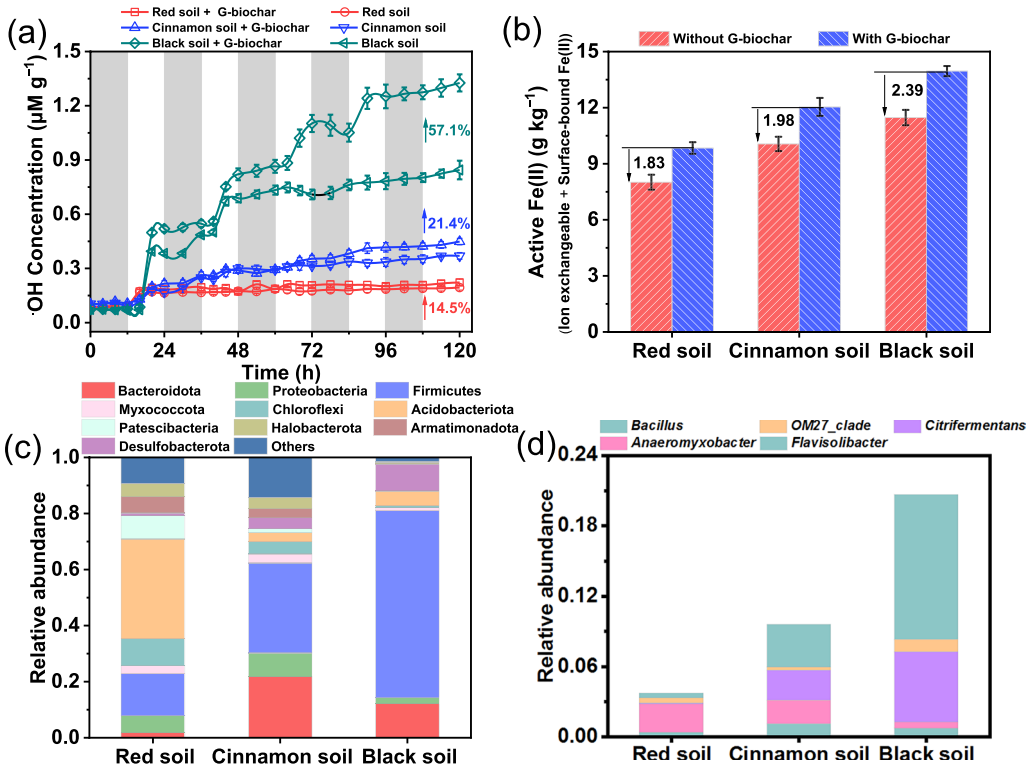

Fig. 5 •OH formation and Fe(II) species transformation in various paddy soils amended with G-biochar. **a** •OH accumulation in red soil, cinnamon soil, and black soil amended with G-biochar during redox fluctuation [dose of G-biochar sample = 10 g kg^{-1}, pH = 5.0, soil to water ratio: 1/5 (w/w)]. **b** Comparison of active Fe(II) contents in various paddy soils with and without G-biochar after 120 h, reaction. **c** Relative abundance of total bacterial communities at the phylum level in various paddy soils. **d** Relative abundance of identified Fe(III)-reducing bacteria at the genus level in various paddy soils

Fe(III)-reducing bacteria (*Bacillus*, *Anaeromyxobacter*, *Flavisolibacter*, and *Citrifermentans*) from the red to black soil (Fig. 5d and S17) was consistent with the increase in active Fe(II) species. This demonstrated that the enhanced microbial Fe(III) reduction associated with G-biochar mainly contributed to the increased abundance of Fe(III)-reducing bacteria. Furthermore, the microbial network analysis showed that the positive portions of the linear relationship increased in black soil (Fig. S18, S19, and S20). In particular, keystone taxa in control soils, such as Myxococcota, Firmicutes, and Actinobacteriota, largely shifted to, for example, Acidobacteriota, Proteobacteria, and Desulfobacterota in soils with G-biochar. This suggests that differences in microbial network relationships could promote Fe(III)-reducing bacterial abundance. In addition, the abundance of Fe(III)-reducing bacteria (*Bacillus*, *Anaeromyxobacter*, *Flavisolibacter*, and *Citrifermentans*) was affected by soil properties [soil organic carbon (SOC), total Fe, pH, active Fe(II), and soil organic matter (SOM) levels] (Fig. S21). The abundance of reducing bacteria (*Bacillus*, *Citrifermentans*, and *Flavisolibacter*) was positively correlated with SOC, pH, and active Fe(II) levels, and negatively correlated with total Fe concentration. The abundance of reducing bacteria (*Anaeromyxobacter*) was positively correlated with total Fe and SOM concentrations and negatively correlated with SOC, pH, and active Fe(II) levels. Thus, reducing bacterial activity is greatly affected by different soil properties, in turn affecting Fe(III) reduction and subsequent •OH generation.

4 Conclusions

This study demonstrates that enhancing the graphitized structure of biochar via flash Joule heating fundamentally shifts its role in paddy soil remediation. The resulting highly conductive graphitized biochar (G-biochar), with a 2.64-fold increase in electrical conductivity, overcomes the inherent electron transfer limitations of conventional biochar. This unlocks the geoconductor function, facilitating direct electron transfer between key

Fe(III)-reducing bacteria (*Bacillus*, *Anaeromyxobacter*, *Citrifermentans*, and *Flavisolibacter*) and Fe(III) minerals via an electron self-adaptation pathway. Consequently, microbial Fe(III) reduction was significantly redirected, leading to an 18.9% increase in active Fe(II) generation. This mechanistic improvement directly amplified the production of reactive oxygen species, evidenced by a 54.9% increase in •OH yield. The enhanced oxidative capacity translated to a 57.2% increase in the sulfamethoxazole degradation rate. The efficacy of G-biochar in promoting microbial Fe(III) reduction varied across paddy soils, primarily governed by the activity of the indigenous reducing microbial community. Critically, these findings redefine the biochar trade-off effect in soil microbial-geochemical processes. They establish that the dominant mechanism for optimizing contaminant degradation relies on biochar's geoconductor function to mediate direct electron transfer, rather than its previously emphasized role as a geobattery electron reservoir.

Supplementary Information

The online version contains supplementary material available at https://doi.org/10.1007/s42773-026-00597-w.

Additional file 1.

Acknowledgements
We gratefully appreciate the financial support from the National Natural Science Foundation of China (No. 22276040).

Author contributions
Hua Shang: conceptualization, methodology, investigation, formal analysis, data curation, visualization, and writing – original draft. Chao Jia: resource, supervision, and investigation. Song Wu: investigation and data curation. Ning Chen: visualization and methodology. Yujun Wang: writing – review and editing. Xiangdong Zhu: conceptualization, methodology, formal analysis, data curation, supervision, funding acquisition, and writing – review and editing.

Funding
This work was supported by the National Natural Science Foundation of China (No. 22276040).

Data availability
The datasets used or analyzed during the current study are available from the corresponding author upon reasonable request.

Declarations

Competing interests
Yujun Wang is an EBM of the journal Biochar, and he was not involved in the peer-review or handling of the manuscript. The authors declare that they have no known competing financial interests or personal relationships that could have appeared to influence the work reported in this paper.

Author details
[1]Biofuels Institute, School of the Environment and Safety Engineering, Jiangsu University, Zhenjiang 212013, China. [2]State Key Laboratory of Soil and Sustainable Agriculture, Institute of Soil Science, Chinese Academy of Sciences, Nanjing 210008, China.

Received: 28 July 2025 Revised: 18 December 2025 Accepted: 21 February 2026
Published online: 17 April 2026

References

Barbhuiya NH, Kumar A, Singh A, Chandel MK, Arnusch CJ, Tour JM, Singh SP (2021) The future of flash graphene for the sustainable management of solid waste. ACS Nano 15:15461–15470
Chen N, Fu Q, Wu T, Cui P, Fang G, Liu C, Chen C, Liu G, Wang W, Wang D, Wang P, Zhou D (2021) Active iron phases regulate the abiotic transformation of organic carbon during redox fluctuation cycles of paddy soil. Environ Sci Technol 55:14281–14293
Chen N, Huang D, Zeng Y, Wang J, Liu G, Liu X, Wu T, Gao Y, Fang G, Wang Y, Zhou D (2024a) Long-term application of agricultural amendments regulate hydroxyl radicals production during oxygenation of paddy soils. Environ Sci Technol 58:13509–13520
Chen X, Song Y, Ling C, Shen Y, Zhan X, Xing B (2024b) Fate of emerging antibiotics in soil-plant systems: a case on fluoroquinolones. Sci Total Environ 951: 75487
Ginn B, Meile C, Wilmoth J, Tang Y, Thompson A (2017) Rapid iron reduction rates are stimulated by high-amplitude redox fluctuations in a tropical forest soil. Environ Sci Technol 51:3250–3259
Gligorovski S, Strekowski R, Barbati S, Vione D (2015) Environmental implications of hydroxyl radicals (• OH). Chem Rev 115:13051–13092
Huang D, Chen N, Zhu C, Sun H, Fang G, Zhou D (2023) Dynamic production of hydroxyl radicals during the flooding–drainage process of paddy soil: an in situ column study. Environ Sci Technol 57:16340–16347
Lee S-H, Hwang Y-M, Byun T-S, Ko J-H, Roh J-S (2023) Effect of heating rate, temperature, and residence time during graphitization on the mechanical and electrical properties of isotropic graphite blocks. Carbon 208:443–451
Li X, Tan M, Wu B, Wang J, Ma J, Chen B, Chu C (2024) Redox oscillation-driven production of reactive oxygen species from black carbon. Environ Sci Technol 58:21210–21217
Liu F, Ding Y, Liu J, Latif J, Qin J, Tian S, Sun S, Guan B, Zhu K, Jia H (2024) The effect of redox fluctuation on carbon mineralization in riparian soil: an analysis of the hotspot zone of reactive oxygen species production. Water Res 265:122294
Luong DX, Bets KV, Algozeeb WA, Stanford MG, Kittrell C, Chen W, Salvatierra RV, Ren M, McHugh EA, Advincula PA (2020) Gram-scale bottom-up flash graphene synthesis. Nature 577:647–651
Page SE, Sander M, Arnold WA, McNeill K (2012) Hydroxyl radical formation upon oxidation of reduced humic acids by oxygen in the dark. Environ Sci Technol 46:1590–1597
Page SE, Kling GW, Sander M, Harrold KH, Logan JR, McNeill K, Cory RM (2013) Dark formation of hydroxyl radical in arctic soil and surface waters. Environ Sci Technol 47:12860–12867
Pan M, Chu LM (2016) Adsorption and degradation of five selected antibiotics in agricultural soil. Sci Total Environ 545:48–56
Qiu C, Jiang L, Gao Y, Sheng L (2023) Effects of oxygen-containing functional groups on carbon materials in supercapacitors: a review. Mater des 230:111952
Shen L, Zhu X, Jiang H, Zhang J, Chen C, R. Reinfelder J, Kappler A, Fang L, Liu T, Liu C, Wu Y, Li F (2025) Physical contact between bacteria and carbonaceous materials: the key switch triggering activated carbon and biochar to promote microbial iron reduction. Environ Sci Technol 59:9576–9586
Strauss V, Marsh K, Kowal MD, El Kady M, Kaner RB (2018) A simple route to porous graphene from carbon nanodots for supercapacitor applications. Adv Mater 30:1704449
Sun T, Levin BDA, Guzman JJL, Enders A, Muller DA, Angenent LT, Lehmann J (2017) Rapid electron transfer by the carbon matrix in natural pyrogenic carbon. Nat Commun 8:14873
Sun T, Levin BDA, Schmidt MP, Guzman JJL, Enders A, Martínez CE, Muller DA, Angenent LT, Lehmann J (2018) Simultaneous quantification of electron transfer by carbon matrices and functional groups in pyrogenic carbon. Environ Sci Technol 52:8538–8547
Teng T, Wu X, Lu Y, Yu F, Jia C, Sun L, Lin L, He Z, Gao J, Zhang S (2023) Flash reforming pyrogenic carbon to graphene for boosting advanced oxidation reaction. Adv Mater Technol 8:2300236

Tong M, Yuan S, Ma S, Jin M, Liu D, Cheng D, Liu X, Gan Y, Wang Y (2016) Production of abundant hydroxyl radicals from oxygenation of subsurface sediments. Environ Sci Technol 50:214–221
Wang B, Wolfe DE, Terrones M, Haque MA, Ganguly S, Roy AK (2017) Electro-graphitization and exfoliation of graphene on carbon nanofibers. Carbon 117:201–207
Wei L, Ge T, Zhu Z, Luo Y, Yang Y, Xiao M, Yan Z, Li Y, Wu J, Kuzyakov Y (2021) Comparing carbon and nitrogen stocks in paddy and upland soils: accumulation, stabilization mechanisms, and environmental drivers. Geoderma 398:115121
Wu S, Fang G, Wang Y, Zheng Y, Wang C, Zhao F, Jaisi DP, Zhou D (2017) Redox-active oxygen-containing functional groups in activated carbon facilitate microbial reduction of ferrihydrite. Environ Sci Technol 51:9709–9717
Wu S, Wang D, Liu C, Fang G, Sun T-R, Cui P, Yan H, Wang Y, Zhou D (2021) Pyridinic- and pyrrolic nitrogen in pyrogenic carbon improves electron shuttling during microbial Fe(III) reduction. ACS Earth Space Chem 5:900–909
Wu NN, Liu S, Xu R, Huang QY, Pan YF, Li HX, Lin L, Hou R, Cheng YY, Xu XR (2024a) New insight into the bioaccumulation and trophic transfer of free and conjugated antibiotics in an estuarine food web based on multimedia fate and model simulation. J Hazard Mater 465:133088
Wu Y, Zhu Z, Sun P, Zhao Z, Zheng X, Long M, Chen Y (2024b) Enhanced short-chain fatty acids production from food waste with magnetic biochar via anaerobic fermentation: linking interfacial, extracellular, and intracellular electron transfer. Chem Eng J 488:150853
Xu H, Hei S, Fu W, Zhang X, Liang P, Pan B, Huang X (2025) Unraveling the trade-off effect of pyrogenic carbons between biopseudocapacitors and bioconductors during anaerobic methanogenesis. Environ Sci Technol 59:2861–2874
Yang Z, Sun T, Kleindienst S, Straub D, Kretzschmar R, Angenent LT, Kappler A (2021) A coupled function of biochar as geobattery and geoconductor leads to stimulation of microbial Fe (III) reduction and methanogenesis in a paddy soil enrichment culture. Soil Biol Biochem 163:108446
Yang P, Wang S, Sun T, Jiang T, Cui Y, Liu G, Guo Y, Liu Y, Hu L, Shi J, Zhang Q, Yin Y, Cai Y, Jiang G (2024) Fire-induced multiple changes in electron transfer properties of peat soil organic matter: the role of functional groups, graphitic carbon, and iron. Environ Sci Technol 58:20457–20467
Yu W, Chu C, Chen B (2022) Enhanced microbial ferrihydrite reduction by pyrogenic carbon: impact of graphitic structures. Environ Sci Technol 56:239–250
Yu F, Jia C, Wu X, Sun L, Shi Z, Teng T, Lin L, He Z, Gao J, Zhang S (2023a) Rapid self-heating synthesis of Fe-based nanomaterial catalyst for advanced oxidation. Nat Commun 14:4975
Yu W, Chu C, Chen B (2023b) Pyrogenic carbon improves Cd retention during microbial transformation of ferrihydrite under varying redox conditions. Environ Sci Technol 57:7875–7885
Yuan S, Liu X, Liao W, Zhang P, Wang X, Tong M (2018) Mechanisms of electron transfer from structrual Fe (II) in reduced nontronite to oxygen for production of hydroxyl radicals. Geochim Cosmochim Acta 223:422–436
Zeng Q, Wang X, Liu X, Huang L, Hu J, Chu R, Tolic N, Dong H (2020) Mutual interactions between reduced Fe-bearing clay minerals and humic acids under dark, oxygenated conditions: hydroxyl radical generation and humic acid transformation. Environ Sci Technol 54:15013–15023
Zhang P, Yuan S, Liao P (2016) Mechanisms of hydroxyl radical production from abiotic oxidation of pyrite under acidic conditions. Geochim Cosmochim Acta 172:444–457
Zhang J, Xu X, Liang J, Huang W, Zhao L, Qiu H, Cao X (2024) Natural attenuation of 2, 4-dichlorophenol in Fe-rich soil during redox oscillations: anoxic–oxic coupling mechanism. Environ Sci Technol 58:13467–13477
Zhou GW, Yang XR, Sun AQ, Li H, Lassen SB, Zheng BX, Zhu YG (2019) Mobile incubator for iron(III) reduction in the gut of the soil-feeding earthworm *Pheretima guillelmi* and interaction with denitrification. Environ Sci Technol 53:4215–4223
Zhou G, Chen L, Zhang C, Ma D, Zhang J (2023) Bacteria–virus interactions are more crucial in soil organic carbon storage than iron protection in biochar-amended paddy soils. Environ Sci Technol 57:19713–19722
Zhu D, Wu H, Fong WK, Tabor RF, Zhang J (2025) The ratio of sp^2 and sp^3 hybridized carbon determines the performance of carbon-based catalysts in H_2O_2 electrosynthesis from O_2. Angew Chem Int Ed 64:e202500145